except that one solves differential equations with the additional constants R_{230} and R_{234}

$$\frac{dN_{230}}{dT} = \lambda_{234}N_{234} - \lambda_{230}N_{230} + R_{230} \qquad (3)$$

$$\frac{dN_{234}}{dT} = \lambda_{238}N_{238} - \lambda_{234}N_{234} + R_{234} \qquad (4)$$

where T is time and N refers to the number of atoms per unit mass of the isotope indicated. Equations 1 and 2 were determined by integration of Eqs. 3 and 4 with the initial condition that $^{230}\text{Th}/^{238}\text{U} = 0$ at $T = 0$. We solved for R_{234} and R_{230} with sample VA-1, using its measured isotopic composition (*4, 5*) (Fig. 2) for δ^{234}U and [^{230}Th/^{238}U] and its uranium-helium age ($T = 520$ ka) [M. L. Bender *et al.*, *Geol. Soc. Am. Bull.* **90**, 577 (1979)] for T. We chose this sample because its isotopic composition is clearly the result of alteration, as it lies outside the range of isotopic compositions possible through closed-system evolution (*5*). For VA-1, R_{234} and R_{230} are 133,000 and 94,300 atoms per year per gram of coral, respectively. It is surprising that R_{234} and R_{230} are similar, given that uranium tends to be soluble and thorium insoluble in natural waters. In theory, redistribution of nuclides would rely on transport by ground water, yet the results of the model suggest the differential solubilities of uranium and thorium do not play a significant role in how they are transported and deposited. It may be that the nuclides are transported on particles in the water, such as organic colloids, which may be more likely to attract uranium and thorium in equal proportions [see J. K. Osmond and M. Ivanovich, in *Uranium-Series Disequilibrium: Applications to Earth, Marine, and Environmental Sciences*, M. Ivanovich and R. S. Harmon, Eds. (Clarendon, Oxford, 1992), pp. 259–289].

22. Deviations from a calculated trend may result from inaccuracies in model assumptions or from true differences in age between samples from a given terrace.
23. Sample UWI-2 crops out in the Rendezvous Hill Terrace, 33 m below its crest. The ^{230}Th age of 129.1 ± 0.8 ka indicates it grew at about the time of the last interglacial period. The sample is either (i) part of a slump, (ii) from a relatively low sea level between two possible last-interglacial sea-level highs (*19*), or (iii) from the sea-level rise immediately before the last interglacial period. To distinguish among these possibilities, similar deposits with clearer stratigraphic relationships must be studied.
24. The uplift rate is calculated by subtracting the estimated maximum eustatic sea level during the last interglacial, 2 to 8 m above present sea level (*10, 26*), from the present height of the last-interglacial terrace and dividing by the age. To calculate the original height of a given deposit, we determine the amount of uplift by multiplying its age by the uplift rate and subtracting the product from its present elevation. This calculation assumes constant uplift. Errors in calculated paleo–sea levels are based on a quadratic combination of errors in the initial height of the last-interglacial terrace [5 ± 3 m above present sea level (*26*)] and in the measured elevations of the samples. Sample WAN-D-3 is not in Table 2, but it also contains paleo–sea level information. It has a ^{230}Th age of 229.5 ± 4.3 ka with an initial δ^{234}U of 191 ± 4, a value outside the range of accuracy by our criterion. However, given the trend of the coral data in Fig. 2, WAN-D-3 is likely older than 200 ka. Using its present height and an age of 215 ± 15 ka to bracket its plausible age, we calculate an initial sea level of 28 ± 9 m below the present level. Thus, it seems likely that terrace WAN-D correlates with and constrains sea-level elevation for one of the stadials in oxygen isotope stage 7, possibly substage 7.2.
25. D. A. Richards, P. L. Smart, R. L. Edwards, *Eos* **73**, 172 (1992); *Nature*, in press.
26. T.-L. Ku, M. A. Kimmel, W. H. Easton, T. J. O'Neil, *Science* **183**, 959 (1974); J. F. Marshall and B. G. Thom, *Nature* **263**, 120 (1976).
27. E. Bard, B. Hamelin, R. G. Fairbanks, A. Zindler, *Nature* **345**, 405 (1990); E. Bard *et al.*, *Nuclear Instrum. Methods Phys. Rev. Sect. B* **52**, 461 (1990); E. Bard, M. Arnold, R. G. Fairbanks, B. Hamelin, *Radiocarbon* **35**, 191 (1993).
28. We have included Bahamian data in our analysis because the Bahamas have a climate similar to that of Barbados. We have not included data from Papua New Guinea (*15, 19*), which include nominal last-interglacial ages as old as 134 ka, or from Hateruma Atoll (*20*) because samples from these localities have initial δ^{234}U values both higher and lower than the modern value [(*15, 19, 20*); C. D. Gallup and R. L. Edwards, unpublished data] that lack consistent isotopic trends, suggesting more complex diagenetic processes than we have modeled. These complex processes may be a result of the high annual rainfall these areas receive.
29. Data for which the nominal initial δ^{234}U value is less than or equal to 158 meet our criterion.
30. W. S. Broecker and G. H. Denton, *Geochim. Cosmochim. Acta* **53**, 2465 (1989).
31. I. J. Winograd *et al.*, *Science* **258**, 255 (1992); K. R. Ludwig *et al.*, *ibid.*, p. 284.
32. The ice volume before a given high-sea-level event may be one of these factors, for example; W. R. Peltier and W. T. Hyde, *J. Atmos. Sci.* **44**, 1351 (1986).
33. J. Imbrie *et al.*, in *Milankovitch and Climate: Part 1*, A. Berger, J. Imbrie, G. Kukla, B. Saltzman, Eds. (Reidel, Dordrecht, Netherlands, 1984), pp. 269–306.
34. See A. Kaufman, *Quat. Res.* **25**, 55 (1986) for review; R. G. Johnson, *Geology* **19**, 686 (1991).
35. A. L. Bloom, W. S. Broecker, J. M. A. Chappell, R. K. Matthews, K. J. Mesolella, *Quat. Res.* **4**, 185 (1974).
36. R. L. Edwards and C. D. Gallup, *Science* **259**, 1626 (1993); K. R. Ludwig, K. R. Simmons, I. J. Winograd, B. J. Szabo, A. C. Riggs, *ibid.*, p. 1626; N. J. Shackleton, *Nature* **362**, 596 (1993); K. R. Ludwig *et al.*, *ibid.*, p. 596.
37. J. Imbrie, A. C. Mix, D. Martinson, *Nature* **363**, 531 (1993); R. G. Johnson and H. E. Wright Jr., *Science* **246**, 262 (1989); I. J. Winograd and T. B. Coplen, *ibid.*, p. 262.
38. J. D. Humphrey, *Sedimentology* **35**, 327 (1988).
39. A. Kaufman and W. S. Broecker, *J. Geophys. Res.* **70**, 4039 (1965).
40. R. G. Lighty, I. G. MacIntyre, R. Stuckenrath, *Nature* **276**, 59 (1978).

41. We thank M. Hinds for sharing her thorough knowledge of Barbados, D. Herbert for assistance in the field, M. K. Reagan, J. L. Banner, D. A. Richards, H. E. Wright Jr., J. W. Beck, K. R. Miller, and F. W. Taylor for insightful comments and discussions, the reviewers for helpful comments, and R. K. Matthews for sample AFM-20. Supported by National Geographic Society (4481-91 and 4887-92), the National Science Foundation (EAR-8904705, EAR-8904895, ATM-8921760, and EAR-8817260 for the TIMS facility), and the University of Minnesota.

2 July 1993; accepted 13 December 1993

Nanowire Array Composites

C. A. Huber,* T. E. Huber, M. Sadoqi,
J. A. Lubin, S. Manalis, C. B. Prater

Long, nanometer-size metallic wires can be synthesized by injection of the conducting melt into nanochannel insulating plates. Large-area arrays of parallel wires 200 nanometers in diameter and 50 micrometers long with a packing density of 5 × 10^8 per square centimeter have been fabricated in this way. When charged, the ends of the wires generate strong, short-range electric fields. The nanowire electric fields have been imaged at high spatial resolution with a scanning force microscope.

The design of composite materials consisting of a mixture of various phases in the nanometer size range has flourished in the last few years (*1, 2*). The bulk electronic and optical properties of such nanocomposites can be tailored by altering the constituents, their size and shape distributions, or their relative concentrations. We describe a class of composites consisting of a high-density array of parallel, nanometer-size, metallic wires embedded in a dielectric matrix. The composite preparation makes use of porous insulators with a regular nanochannel structure as host or template. The small channels in the host are filled with the conducting phase by high-pressure injection of its melt (*3, 4*). In contrast to other microporous materials, such as the silica glasses of the Vycor type, which support a random network of pores, the regular nanochannel matrices allow for the preparation of nanocomposites whose physical properties are easier to interpret and

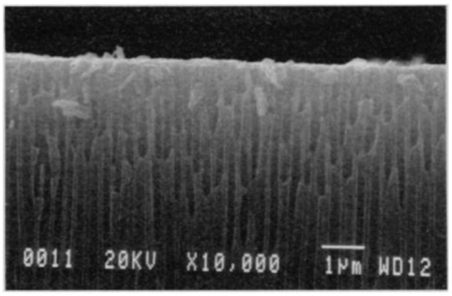

Fig. 1. Cross section of the top surface of an alumina with 200-nm nominal channel diameter, obtained by cleavage of the plate.

C. A. Huber, Research and Technology Department, Naval Surface Warfare Center, Silver Spring, MD 20903, USA.
T. E. Huber and M. Sadoqi, Department of Physics, Polytechnic University, Brooklyn, NY 11201, USA.
J. A. Lubin, Laser Chemistry, Howard University, Washington, DC 20059, USA.
S. Manalis and C. B. Prater, Digital Instruments, Santa Barbara, CA 93103, USA.

*To whom correspondence should be addressed.

more amenable to theoretical treatments.

The template strategy has been successfully used by others to chemically synthesize semiconductor and metal nanoparticles in microporous dielectrics (*5–7*) and in the cavities of zeolites (*8*). More recently, experiments on capillary-induced filling of carbon nanotubes with lead have been reported (*9*). In those cases, the active conducting phase occupies a volume fraction typically less than 1%. The injection technique can produce the dense nanocomposites required for applications involving electrical transport.

The nanowire composites can be used as building blocks for high-density electrical multifeedthroughs and photosensing arrays. Also, the electrically conductive composites can be microengineered to become optically transmissive (*10*). Electrical characterization of the nanowires by conventional four-point probe resistance measurements are precluded in our case because the wires are perpendicular to the exposed macroscopic surfaces. Instead, we developed a scanning force microscope technique to map the electric fields generated by the nanowires.

The channel matrix used for the synthesis of the nanowire composite is an inorganic matrix commercially sold for microfiltration under the trade name Anopore (*11*). It consists of an Al_2O_3 plate 25 mm in diameter and about 55 µm thick, which supports an array of parallel, noninterconnected, cylindrical channels running perpendicular to the plate surface. A photograph of a plate of 200-nm nominal channel diameter and about 50% porosity taken with a scanning electron microscope (Fig. 1) illustrates the tubular channels. From analysis of micrographs of the plate top surface, we determined a channel diameter of 258 ± 46 nm and a channel density of 5×10^8 to 7×10^8 cm^{-2}. The nanochannel Al_2O_3 plates are prepared by the anodic oxidation of aluminum. The channel diameter and channel density are controlled by the choice of electrolyte and by the anodizing voltage (*12*). The channel structure is slightly asymmetric, with the channels branching and tapering toward the plate surface that was originally in contact with the aluminum metal. This asymmetry is not a problem because the thickness over which the smaller channels extend is on the order of 0.5 µm, which is easily removed by mechanical polishing. The ability of the nanochannel matrix to withstand high temperatures is essential to the composite preparation process. We have heated the Al_2O_3 plates up to 800°C without observing any change in the microstructure.

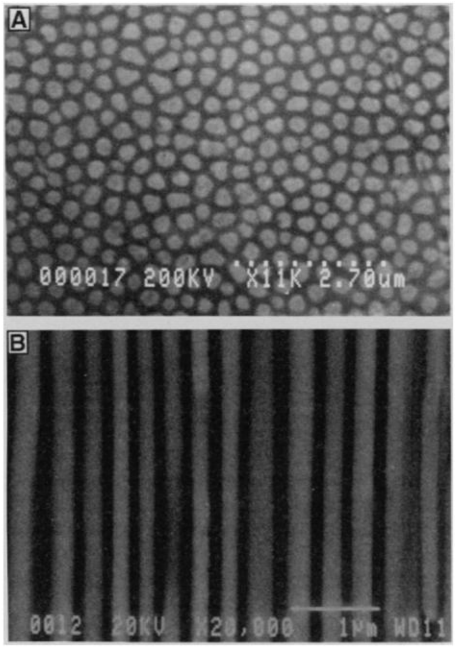

Fig. 2. A Te nanowire composite prepared from a 200-nm-channel alumina plate. (**A**) Top view and (**B**) cross section of a 50-µm-thick plate that was cleaved and mechanically polished. In (B), contrast between Te (light) and Al_2O_3 (dark) was enhanced by imaging of the backscattered electrons, which result mostly from the Te, with its higher atomic number.

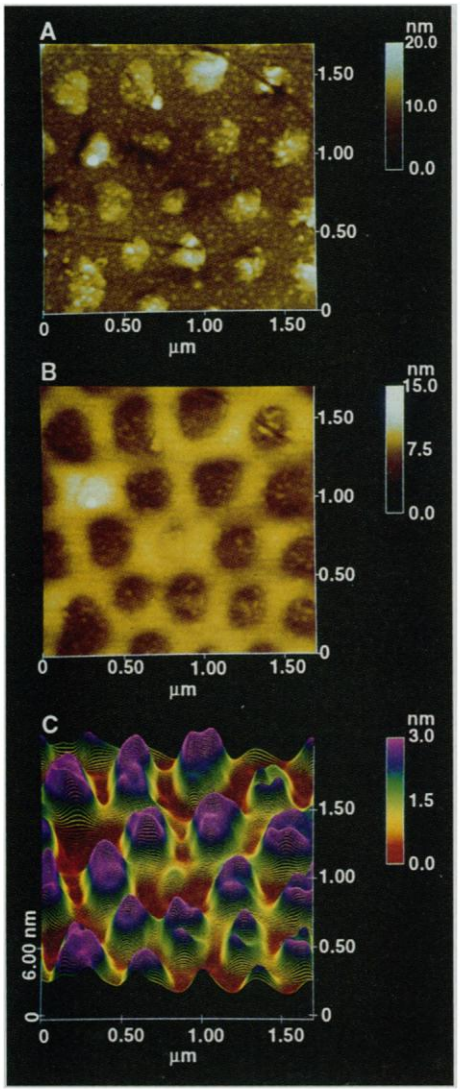

Fig. 3. (**A**) Topographic image of the nanowire composite; the Al_2O_3 has been etched so that the wires protrude slightly. Higher topography features appear lighter. Dark lines are scratches from mechanical polishing. (**B**) Corresponding image of electric force gradient, taken with a lift height of 30 nm. The vertical scale shows the amplitude of the cantilever oscillations. The strong electric force signal appearing as a bright spot is probably caused by a large electrostatic charge on the particle shown at this location in (A). (**C**) Contours of constant electric force gradient. The oscillation amplitude scale has been inverted with respect to (B).

For the various metals and semiconductors we have investigated, an externally applied hydrostatic pressure is needed to overcome surface tension effects, which prevent the melt from entering the narrow channels of insulating hosts. An estimate for the diameter D of the smallest channel filled at pressure P can be obtained from the Washburn equation: $D = -4\gamma\cos\theta/P$, where γ is the surface tension of the liquid and θ is the contact angle between the liquid and the insulator ($\theta > 90°$ for nonwetting liquids). Values for the surface tension of some liquid metals and semiconductors of interest span the 100 to 600 dyne/cm range. Assuming a mid-range surface tension of 300 dyne/cm and the least favorable case of complete nonwetting ($\theta = 180°$), the Washburn equation becomes $D = 12/P$, where P is measured in kilobars and D is in nanometers. For a modest applied pressure of 4 kbar, for example, all channels larger than 3 nm in diameter will fill with metal.

For the injection process, the nanochannel alumina and the material to be injected are cleaned and packed in a thin-wall metal tube sealed at one end; the other end is connected to a vacuum system. The assembly is then vacuum-dried in an oven for several hours at a temperature slightly below the melting point of the injecting material. After cooling to room temperature, the metal tube is backfilled with an inert gas and sealed at the other end. The metal ampoule is then inserted into the reactor of a high temperature–high pressure injection apparatus. The design and operation of the apparatus have been described elsewhere (*4*). Briefly, the reactor is first heated to a temperature above the melting point of the impregnant. The pressure is then gradually raised, collapsing the metal ampoule and forcing the molten material into the matrix channels. When the injection is complete, the reactor is cooled and the impregnant solidifies inside the channels, the pressure is then released. The sample is extracted from the ampoule and cleaned of the surrounding excess impregnant by standard mechanical polishing techniques. In this way, we prepared nanowires of various metals (In, Sn, and Al) and semiconductors (Se, Te, GaSb, and Bi_2Te_3) (Fig. 2).

The nanowire composites create substantial electric field patterns over the sample surface. We used a scanning probe microscope to measure electric fields at the surface of a nanocomposite. In a NanoScope (Digital Instruments, Santa Barbara, California) scanning force microscope, the sample is mounted with conductive epoxy to a metal holder and is held at a few volts relative to a conductive cantilever tip that is grounded. The metal-coated, etched, single-crystal silicon tip has a radius of curvature of about 5 nm. The tip is set to oscillate at a frequency near its resonance frequency (78 kHz). When the cantilever encounters a vertical electric field gradient, the effective spring constant is modified, shifting its resonance frequency. By recording the amplitude of the cantilever oscillations while scanning the sample surface, we obtain an image that reveals the strength of the electric force gradient (*13, 14*).

The image, however, may also contain topographical information; it is difficult to separate the two effects. This is circumvented by taking measurements in two passes over each scan line (*15*). On the first pass, a topographical image (Fig. 3A) is taken with the cantilever tapping the surface, and the information is stored in memory. On the second pass, the tip is lifted to a selected separation between the tip and local surface topography (typically 20 to 200 nm), such that the tip does not touch the surface. By using the stored topographical data instead of the standard feedback, we can keep the separation constant. In this second pass, cantilever oscillation amplitudes are sensitive to electric force gradients without being influenced by topographic features (Fig. 3B). This two-pass measurement process is recorded for every scan line, producing separate topographic and electric force images. From these images, contours of electric force gradient (Fig. 3C) can be drawn.

The amplitude of the cantilever oscillations is very large for small lift heights, and the images fade at separations larger than 80 nm. This is consistent with previous reports of a strong dependence of the tip-surface force on the vertical separation (*13*). More work needs to be done to understand this quantitatively. Note that some of the nanowires that appear in the topographic image are missing from the electric field image (Fig. 3). This is because either electrical contact to these nanowires has failed or electrical conduction along the wire length has been interrupted. The scanning force technique thus provides a unique way of mapping the electrical properties of nanocomposites.

Applications of the metal nanowire composites include high-density electrical multifeedthroughs and high-resolution plates for transferring a two-dimensional charge distribution between microelectronic devices. The semiconductor nanowires can be used in photodetector arrays of high spatial resolution, where each wire acts as a pixel of submicrometer dimensions. Also, with the application of the injection technique to ultrasmall channel insulators (channel diameter less than 50 nm) (*16, 17*), nanowire arrays can be made for fundamental studies of a variety of phenomena, such as quantum confinement of charge carriers and mesoscopic transport.

REFERENCES AND NOTES

1. An overview can be found in M. J. Yacaman, T. Tsakalakos, B. H. Kear, Eds., *Nanostruct. Mat.* **3** (nos. 1–6) (1993).
2. R. Roy, *Nanophase and Nanocomposite Materials*, S. Komarneni, J. C. Parker, G. J. Thomas, Eds. (Mat. Res. Soc. Symp. Proc. 286, Materials Research Society, Pittsburgh, PA, 1993), pp. 241–250, and references therein.
3. Early work on the preparation of ultrathin superconducting wires by injection of nanochannel matrices was done by W. G. Schmidt and R. J. Charles [*J. Appl. Phys.* **35**, 2552 (1964)] and by V. N. Bogomolov [*Sov. Phys. Usp.* **21**, 77 (1978)].
4. C. A. Huber and T. E. Huber, *J. Appl. Phys.* **64**, 6588 (1988).
5. N. F. Borrelli and J. C. Luong, *Proc. SPIE* **866**, 104 (1988).
6. B. L. Justus, R. J. Tonucci, A. D. Berry, *Appl. Phys. Lett.* **61**, 3151 (1992).
7. M. J. Tierney and C. R. Martin, *J. Phys. Chem.* **93**, 2878 (1989).
8. G. D. Stucky and J. E. Mac Dougall, *Science* **247**, 669 (1990), and references therein.
9. P. M. Ajayan and S. Iijima, *Nature* **361**, 333 (1993).
10. An array of parallel metal cylinders would be transparent to light that had a wavelength much larger than the cylinder diameter and separation and propagated along the cylinder axis [D. E. Aspnes, A. Heller, J. D. Porter, *J. Appl. Phys.* **60**, 3028 (1986)].
11. Whatman Laboratory Division, Clifton, NJ.
12. J. W. Diggle, T. C. Downie, C. W. Goulding, *J. Electrochem. Soc.* **69**, 365 (1969).
13. Y. Martin, D. W. Abraham, H. K. Wickramasinghe, *Appl. Phys. Lett.* **52**, 1103 (1988).
14. J. E. Stern, B. D. Terris, H. J. Maimin, D. Rugar, *ibid.* **53**, 2717 (1988).
15. Lift Mode operation, Digital Instruments, Inc., Santa Barbara, CA (patent pending).
16. R. C. Furneaux, W. R. Rigby, A. P. Davidson, *Nature* **337**, 147 (1989).
17. R. J. Tonucci, B. L. Justus, A. J. Campillo, C. E. Ford, *Science* **258**, 783 (1992).
18. We thank V. Elings for valuable discussions, B. Schardt and S. Thedford for image processing, and S. Nourbakhsh for electron microscopy. This work was supported by the Army Research Office, the Independent Research Program of the Office of Naval Research, and the National Science Foundation.

22 October 1993; accepted 20 December 1993

Green Fluorescent Protein as a Marker for Gene Expression

Martin Chalfie,* Yuan Tu, Ghia Euskirchen, William W. Ward, Douglas C. Prasher†

A complementary DNA for the *Aequorea victoria* green fluorescent protein (GFP) produces a fluorescent product when expressed in prokaryotic (*Escherichia coli*) or eukaryotic (*Caenorhabditis elegans*) cells. Because exogenous substrates and cofactors are not required for this fluorescence, GFP expression can be used to monitor gene expression and protein localization in living organisms.

Light is produced by the bioluminescent jellyfish *Aequorea victoria* when calcium binds to the photoprotein aequorin (*1*). Although activation of aequorin in vitro or in heterologous cells produces blue light, the jellyfish produces green light. This light is the result of a second protein in *A. victoria* that derives its excitation energy from aequorin (*2*), the green fluorescent protein (GFP).

Purified GFP, a protein of 238 amino acids (*3*), absorbs blue light (maximally at 395 nm with a minor peak at 470 nm) and emits green light (peak emission at 509 nm with a shoulder at 540 nm) (*2, 4*). This fluorescence is very stable, and virtually no photobleaching is observed (*5*). Although the intact protein is needed for fluorescence, the same absorption spectral properties found in the denatured protein are found in a hexapeptide that starts at amino acid 64 (*6, 7*). The GFP chromophore is derived from the primary amino acid sequence through the cyclization of serine-dehydrotyrosine-glycine within this hexapeptide (*7*). The mechanisms that produce the dehydrotyrosine and cyclize the poly-

---

M. Chalfie, Y. Tu, G. Euskirchen, Department of Biological Sciences, Columbia University, New York, NY 10027, USA.

W. W. Ward, Department of Biochemistry and Microbiology, Cook College, Rutgers University, New Brunswick, NJ 08903, USA.

D. C. Prasher, Biology Department, Woods Hole Oceanographic Institution, Woods Hole, MA 02543, USA.

---

*To whom correspondence should be addressed.

†Present address: U.S. Department of Agriculture, Building 1398, Otis Air National Guard Base, MA 02542, USA.